

Article

New Insight into the Interplay of Method of Deposition, Chemical State of Pd, Oxygen Storage Capability and Catalytic Activity of Pd-Containing Perovskite Catalysts for Combustion of Methane

Silva Stanchovska ¹, Georgy Ivanov ¹, Sonya Harizanova ¹, Krasimir Tenchev ² , Ekaterina Zhecheva ¹, Anton Naydenov ^{1,*}  and Radostina Stoyanova ¹ 

¹ Institute of General and Inorganic Chemistry, Bulgarian Academy of Sciences, Acad. G. Bonchev St., Bldg 11, 1113 Sofia, Bulgaria; stanchovska@svr.igic.bas.bg (S.S.); geoivanov@yahoo.com (G.I.); sonya@svr.igic.bas.bg (S.H.); zhecheva@svr.igic.bas.bg (E.Z.); radstoy@svr.igic.bas.bg (R.S.)

² Institute of Catalysis, Bulgarian Academy of Sciences, Acad. G. Bonchev St., Bldg 11, 1113 Sofia, Bulgaria; tenchev@ic.bas.bg

* Correspondence: naydenov@svr.igic.bas.bg; Tel.: +359-02-979-25-36



Citation: Stanchovska, S.; Ivanov, G.; Harizanova, S.; Tenchev, K.; Zhecheva, E.; Naydenov, A.; Stoyanova, R. New Insight into the Interplay of Method of Deposition, Chemical State of Pd, Oxygen Storage Capability and Catalytic Activity of Pd-Containing Perovskite Catalysts for Combustion of Methane. *Catalysts* **2021**, *11*, 1399. <https://doi.org/10.3390/catal11111399>

Academic Editor:
Avelina Garcia-García

Received: 28 October 2021

Accepted: 15 November 2021

Published: 18 November 2021

Publisher's Note: MDPI stays neutral with regard to jurisdictional claims in published maps and institutional affiliations.



Copyright: © 2021 by the authors. Licensee MDPI, Basel, Switzerland. This article is an open access article distributed under the terms and conditions of the Creative Commons Attribution (CC BY) license (<https://creativecommons.org/licenses/by/4.0/>).

Abstract: Elaboration of Pd-supported catalysts for catalytic combustion is, nowadays, considered as an imperative task to reduce the emissions of methane. This study provides new insight into the method of deposition, chemical state of Pd and oxygen storage capability of transition metal ions and their effects on the catalytic reactivity of supported catalysts for the combustion of methane. The catalyst with nominal composition $\text{La}(\text{Co}_{0.8}\text{Ni}_{0.1}\text{Fe}_{0.1})_{0.85}\text{Pd}_{0.15}\text{O}_3$ was supported on SiO_2 -modified/ γ -alumina using two synthetic procedures: (i) aerosol assisted chemical vapor deposition (U-AACVD) and (ii) wet impregnation (Imp). A comparative analysis shows that a higher catalytic activity is established for supported catalyst obtained by wet impregnation, where the PdO-like phase is well dispersed and the transition metal ions display a high oxygen storage capability. The reaction pathway over both catalysts proceeds most probably through Mars–van Krevelen mechanism. The supported catalysts are thermally stable when they are aged at 505 °C for 120 h in air containing 1.2 vol.% water vapor. Furthermore, the experimentally obtained data on $\text{La}(\text{Co}_{0.8}\text{Ni}_{0.1}\text{Fe}_{0.1})_{0.85}\text{Pd}_{0.15}\text{O}_3$ -based catalyst, supported on monolithic substrate VDM[®] Aluchrom Y Hf are simulated by using a two-dimensional heterogeneous model for monolithic reactor in order to predict the performance of an industrial catalytic reactor for abatement of methane emissions.

Keywords: methane; catalytic combustion; palladium; perovskite; Mars-van Krevelen

1. Introduction

Methane is one of the most abundant air pollutants (second after carbon dioxide), responsible for global warming [1,2] which requires the reduction of its emissions. At present time there is an increased interest in the application of methane (as the main component of natural gas) as a fuel in the internal combustion engines. Bordelanne and co-workers [3] reported that GHG emissions from vehicles on compressed natural gas (CNG) fuel may produce significantly lower emissions than of gasoline vehicles and in case of hybrid CNG vehicles the reduction of 51% can be reached. In the case of the Toyota Prius CNG Hybrid prototype fuelled by biomethane produced from waste (in comparison to a gasoline vehicle), the emissions are lowered by 87% [3]. Therefore the use of biomethane can lead to reduction of GHG emissions below the minimum specified by the European Directive on the Promotion of Renewable Energy Sources (2009/28/EC). However, the wide use of methane as a fuel for the internal combustion engines meets problems originating from the unburned methane in the exhaust gases.

One of the methods for abatement of methane is catalytic combustion. Palladium supported catalysts are known to be the most active catalysts, however, the main problem is associated with the deactivation at high temperatures (above 500 °C). Thus, the efforts of the researchers are focused on the improvement of the thermal stability of the catalysts [4–6]. In this respect, perovskite oxides with a general formula ABO_3 represent an alternative of the Pd-based catalysts due to their good thermal and water stability [7]. Barbato et al. [8] and Di Sarli et al. [9] reported significant progress in the application of $LaMnO_3$ -based monoliths for the reaction of methane combustion.

The perovskite structure is flexible, so that it is able to accommodate a variety of transition metal elements on the B-site, as well as to create easily more oxygen vacancies—a phenomenon that allows simply controlling both the redox and oxygen mobility properties of perovskites, which in its turn determines their catalytic activities [10]. Among perovskite series, the highest catalytic activity in CH_4 combustion was established for perovskites containing lanthanum as metal A and Co, Mn, Fe and Ni as metal B [10,11]. The mixing of transition metal ions having different ionic dimensions in the B-site permits to design of both the redox properties and oxygen content of perovskites $AB_{1-x}M_xO_{3\pm\delta}$, as a result of which their catalytic properties are significantly improved (for example, mixed $LaCo_{1-x}Fe/Mn_xO_3$ and double substituted $LaCo_{1-2x}Ni_xFe_xO_3$ perovskites) [12–14].

As in the case of transition metal ions, the B-perovskite site is able to accommodate palladium ions leading to a formation of $AB_{1-x}Pd_xO_3$ with improved catalytic properties. Eyssler et al. [15] demonstrated that Pd can be incorporated into the perovskite structure in the B-site as is the case of Fe and Co ($La(Fe,Pd)O_{3\pm\delta}$ and $La(Co,Pd)O_{3\pm\delta}$) and the highest catalytic activity was found out for the samples, where palladium was predominantly dispersed as supported PdO particles and the Pd incorporation in the perovskite-type lattice may not be favorable for the methane oxidation reaction.

The self-regenerative function was reported for the $LaFe_{0.57}Co_{0.38}Pd_{0.05}O_3$ system, in which palladium oscillates between two oxidation and coordination states depending on the redox reaction conditions [16]. In excess of oxygen the palladium is incorporated in the perovskite lattice as Pd^{3+} (thus occupying the B-sites), while when the reductive reagent prevails, there is a segregation out of the perovskite crystal in the form of metallic palladium. The observed oscillations within the structure, observed even within the temperature range of 100–400 °C [17,18], prevent the agglomeration of palladium.

It was shown that Pd/ γ - Al_2O_3 catalyst loses about 10% of dispersion degree due to the sintering of palladium. At the same time, $LaFe_{0.57}Co_{0.38}Pd_{0.05}O_3$ maintains a high Pd dispersion (particle size of 1–3 nm) and that is because its activity is almost unchanged [16,19]. After the reporting of the self-regenerative behaviour of $LaFe_{0.57}Co_{0.38}Pd_{0.05}O_3$, new “intelligent” catalysts were synthesized based on $LaFeO_3$, $LaAlO_3$, $CaTiO_3$, $CaZrO_3$, $SrTiO_3$, $SrZrO_3$, $BaTiO_3$ and $BaZrO_3$ [20]. Due to the strong metal-support interaction between the noble metal and the perovskite, it is possible to improve the thermal stability, while keeping low noble metal concentration [21,22].

Regarding the experimentally observed reaction kinetics of the methane combustion on palladium catalysts, there is a controversy in the literature: Eley-Rideal (ER), Langmuir-Hinshelwood (LH), Mars van Krevelen (MvK) mechanisms have been proposed, MvK models being the most frequently applied [23]. The reaction kinetics is a result of the competition between the adsorbed oxygen and the lattice oxygen during their participation in the reaction of the methane combustion [24].

Due to the complexity of the perovskite structure and the type of Pd integration, the method of synthesis has a decisive effect on the catalytic performance [25,26]. The most successful methods for the formation of nanostructured catalysts with a high specific surface area are solution-based techniques [25,26]. These techniques are also applicable to the deposition of catalysts over different types of structured surfaces [25]. The development of a suitable preparation method for catalysts deposition is highly needed in respect of the catalysts utilization in different technological sectors.

The aim of the present study was to obtain new data on the preparation and the catalytic behavior of Pd-containing perovskite catalysts supported on SiO₂-modified/ γ -alumina for further application in abatement of methane emissions. The nominal composition of the Pd-containing perovskite La(Co_{0.8}Ni_{0.1}Fe_{0.1})_{0.85}Pd_{0.15}O₃ is selected since nickel and iron ions have opposite effects on the redox properties of cobalt-based perovskite, that allows to modify and improve their catalytic performance, as it was previously shown [13,14]. Regarding the deposition of the catalytically active phase, two synthetic procedures have been applied: (i) impregnation and (ii) aerosol assisted chemical vapor deposition.

2. Results and Discussions

2.1. Structure and Texture of Pd-Containing Perovskite Supported on SiO₂-Modified/ γ -Alumina

The powder X-ray diffraction patterns of deposited catalysts are dominated by diffraction peaks due to γ -alumina support, which makes difficulties in the determination of phase composition. In this case, the more informative is the SEM/EDS study. The deposition of the catalysts on the SiO₂-modified/ γ -alumina proceeds in a different way when the process is carried out by impregnation and by U-AACVD—pyrolysis (Figure 1).

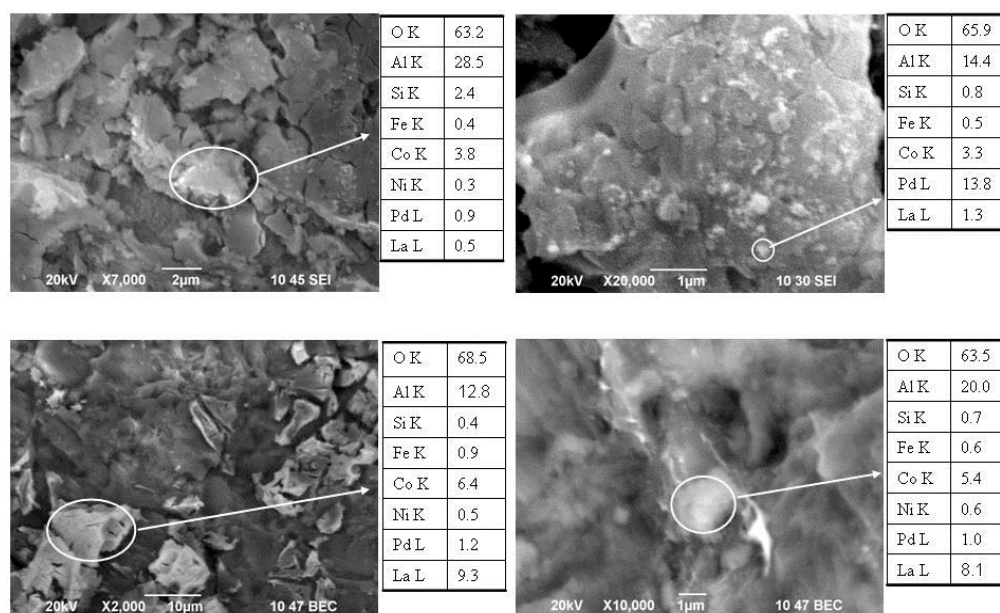


Figure 1. SEM images at different magnifications for Pd-LMO/Imp (top) and Pd-LMO/U-AACVD (bottom). The EDS results are also indicated.

It seems that the impregnation technique leads to a deposition of plate-like aggregates, on the surface of which small particles are visible (Figure 1 top). The distribution of elements in aggregates, determined by EDS, shows that the small particles are mainly composed of Pd, while the aggregates contain all the other elements such as La, Co, Ni, Fe and Pd in ratio, which does not coincide with that for the nominal perovskite composition. This means that the mixture of palladium, lanthanum and transition metal oxides rather than pure perovskite phase is formed during the impregnation technique. It is of importance that the ratio between Si and Al remains constant, thus indicating a homogeneous distribution of SiO₂ over the γ -alumina. The plate-like aggregates are also formed during the U-AACVD—pyrolysis process, but the aggregates are rather non-homogeneously distributed over the surface (Figure 1). The distribution of elements in aggregates corresponds to the requirement for the nominal perovskite composition, i.e., La(Co_{0.8}Ni_{0.1}Fe_{0.1})_{0.85}Pd_{0.15}O₃. Both the SEM images and the EDS analysis reveal that the perovskite phase is mainly deposited over SiO₂-modified/ γ -alumina support during U-AACVD—pyrolysis process, which is an opposite fact to that established for the impregnation process. It is noticeable that, irrespective of the synthesis procedure, the mean

Pd-content in supported catalysts is one and the same: 1.7 ± 0.2 wt % for Pd-LMO/Imp and 1.6 ± 0.4 wt % Pd-LMO/U-AACVD.

The formation of well-dispersed Pd-rich particles is demonstrated by TEM analysis. Figure 2 gives SAED and HRTEM images for Pd-LMO/Imp.

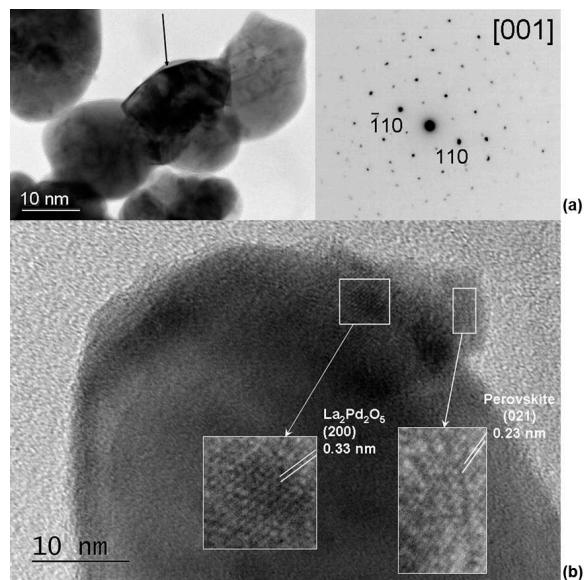


Figure 2. Bright field images and SAED (a), HRTEM (b) of Pd-LMO/Imp.

The SAED of particles with dimensions of about 10 nm displays an occurrence of Pd-rich phases such as La_2PdO_4 . In addition, HRTEM gives an indication that the small particles are composed of domains containing Pd-rich (such as $\text{La}_2\text{Pd}_2\text{O}_5$) and perovskite phases. The same picture is observed with Pd-LMO/U-AACVD sample (not shown here).

The state of Pd species in the supported catalysts is probed by means of XPS. Figure 3 shows the Pd 3d_{3/2} and Pd 3d_{5/2} core levels spectra for the supported catalysts Pd-LMO/Imp and Pd-LMO/U-AACVD.

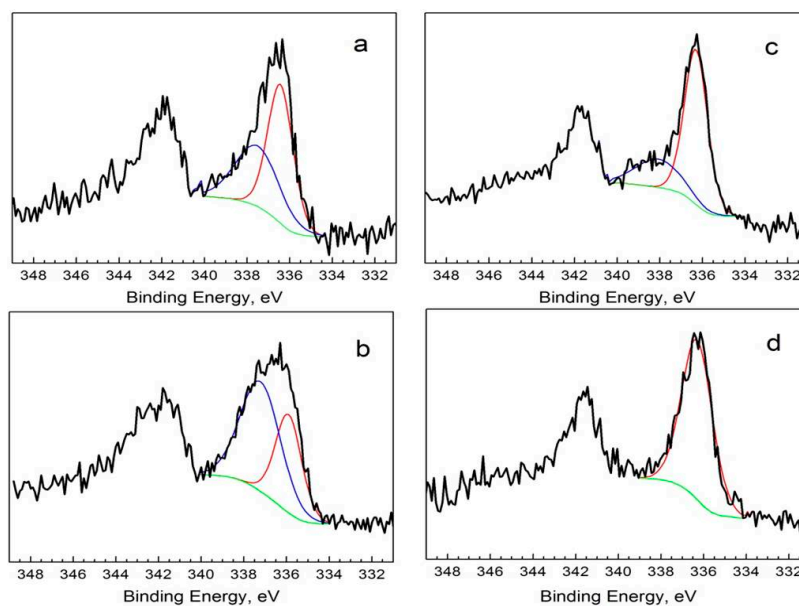


Figure 3. XPS spectra in the Pd 3d_{3/2} and Pd 3d_{5/2} regions for fresh Pd-LMO/Imp (a) and Pd-LMO/U-AACVD (b), as well as for catalytic tested Pd-LMO/Imp (c) and Pd-LMO/U-AACVD (d). The peak deconvolution in the Pd 3d_{5/2} region is indicated with blue and red lines. The Shirley's type of background is also shown (green lines).

The Pd 3d5/2 spectra of both catalysts consist of a broad asymmetric envelope, which can be deconvoluted into two overlapping signals: one narrow signal centered at around 336 eV and other broader signal centered above 337 eV. The deconvoluted parameters including peak position, line width and the ratio between signals are summarized in Table 1. The comparison shows that the positions and the line widths for the two signals are relatively the same for the catalysts prepared by the impregnation and by the U-AACVD—pyrolysis, but the ratio between them displays a clear dependence on the synthesis history: the broad high-energy peak is more intensive for the catalysts obtained by the U-AACVD—pyrolysis, while the narrow low-energy signal—for the impregnated catalysts (Figure 3, Table 1).

Table 1. Pd 3d5/2 binding energies, line width and ratio of the high-energy signal to the low-energy signal (I_{HE}/I_{LE}) for Pd-LMO/Imp and Pd-LMO/U-AACVD in the pristine state and after catalysts test.

Samples	Signal 1		Signal 2		I_{HE}/I_{LE}
	Pd 3d5/2, eV	Line Width, eV	Pd 3d5/2, eV	Line Width, eV	
Pd-LMO/Imp—fresh	336.4	1.40	337.5	2.43	0.76
Pd-LMO/Imp—after catalytic test	336.3	1.28	338.1	2.5	0.36
Pd-LMO/U-AACVD—fresh	335.9	1.45	337.2	2.2	1.67
Pd-LMO/U-AACVD—after catalytic test	336.3	1.69	-	-	0

Based on the numerous XPS studies on the oxidation state of Pd in palladium-containing perovskite powders and catalysts [15,17,27], the broad high energy peak above 337 eV can be assigned to Pd³⁺ or Pd⁴⁺ species inserted inside the B-site of the perovskite structure, whereas the narrow low-energy peak within the range of 335.9–336.4 eV is probably associated with Pd²⁺ in PdO [15,17,27]. The ratio between signals reveals that the surface of impregnated catalysts is enriched with low-oxidized Pd²⁺ ions stabilized in the PdO-like phase, while highly oxidized Pd^{3+/4+} ions included in the perovskite-like phase occur predominantly on the surface of spray-U-AACVDolysed catalysts. The XPS results coincide well with the SEM observation for the deposition of oxide mixture during impregnation, while the Pd-containing perovskite phase is formed after U-AACVD—pyrolysis.

The surface Pd-content in supported catalysts is calculated from corresponding XPS spectra. The results show that the surface Pd-content in two supported catalysts is relatively the same: 4.0 wt % for Pd-LMO/Imp and 4.2 wt % for Pd-LMO/U-AACVD. It is worth mentioning that the surface Pd-content estimated by XPS is higher (more than 2 times) than that determined by EDS analysis, which is a more deeply penetrating method. The difference between XPS and EDS data for Pd content means that the Pd ions occur mainly on the catalyst's surface.

The BET surface area of supported catalysts Pd-LMO/Imp and Pd-LMO/U-AACVD, as well as the supports γ -alumina and SiO₂-modified γ -alumina, is further analyzed by low-temperature nitrogen adsorption. All the samples are mesoporous with predominant pores sizes between 4 and 15 nm, which are demonstrated by the type IV hysteresis loops. The specific surface area, the total pore volume and the mean pore diameter are listed in Table 2. The comparison shows that the texture parameters of γ -Al₂O₃ support are only slightly perturbed after its modification with SiO₂. A tendency for reduction in the surface area and the total pore volume is concomitant with an increase in the mean pore diameter and it is observed during the deposition of Pd-containing perovskites. This trend is more pronounced for the catalysts obtained by the impregnation technique.

The observed texture changes are in good agreement with the morphology observations (Figure 1), where non-homogeneous distribution of supported Pd-containing perovskite is established when the U-AACVD—pyrolysis technique is used. To check this supposition, Table 2 gives also the texture parameters for perovskite supported catalysts without containing any Pd. As in the case of the Pd-containing catalysts, the specific surface area and the total pore volume decrease more strongly for the catalyst obtained by the impregnation.

Table 2. Specific surface area (S), total pore volume (V_t) and mean pore diameter (D) for γ -Al₂O₃, SiO₂-modified γ -Al₂O₃, Pd-LMO/U-AACVD and Pd-LMO/Imp. For comparison, the corresponding perovskites without Pd are also given (LMO/Imp and LMO/U-AACVD, respectively).

Sample	S, m ² /g	V_t , cm ³ /g	D, nm
γ -Al ₂ O ₃	219	0.41	7.4
SiO ₂ modified γ -Al ₂ O ₃	204	0.39	7.8
Pd-LMO/U-AACVD	181	0.37	8.1
Pd-LMO/Imp	172	0.36	8.7
LMO/U-AACVD	164	0.38	9.2
LMO/Imp	153	0.35	9.1

The reducibility of supported catalysts is monitored using temperature programmed reduction with both strong and mild agents such as H₂ and CH₄. Figure 4A compares the H₂-TPR curve profiles for Pd-LMO/Imp and Pd-LMO/U-AACVD samples. The comparison indicates that the reduction of both supported catalysts is accomplished in three steps in the well separated temperature ranges: between 50 and 160 °C, 250 and 470 °C and above 580 °C, respectively. To rationalize the reduction properties of supported Pd-containing catalysts, the same figure demonstrates the H₂-TPR curve for perovskite supported catalyst, which does not contain any Pd, i.e., LMO/Imp. As one can see, the LMO/Imp exhibits only two broad peaks of hydrogen consumption: between 250 and 500 °C and above 550 °C, respectively. This reveals clearly that the low-temperature peaks of hydrogen consumption are related to the Pd species. Depending on the method of synthesis, the Pd-containing catalysts displays in the low temperature range different H₂-TPR curve profiles: Pd-LMO/Imp exhibits one dominating peak of H₂ consumption centred at 72 °C with a shoulder at around 120 °C, while two peaks at 75 °C and 115 °C are clearly resolved for Pd-LMO/U-AACVD. This is a H₂-TPR evidence for the variation in the distribution of Pd species over the supported catalysts. The peak at 75 °C can be attributed to the reduction of dispersed PdO-like phase, while the peak at 115 °C can be interpreted by the reduction of Pd species included inside the perovskite-like phase or by the strong interaction between PdO-like phase with SiO₂-modified alumina support [28,29]. The effect of the synthesis procedure on the distribution of Pd species over the supported catalysts is in good agreement with the above SEM and XPS observations (Figures 1 and 3a,c): the impregnation method yields well dispersed PdO-like phase, while Pd-containing perovskite is a main product during U-AACVD deposition method. It is worth mentioning that the negative peak at around 220 °C (especially pronounced for Pd-LMO/U-AACVD) could be tentatively related to the decomposition of palladium hydride, which is previously observed for PdO-supported Ce, Zr, alumina [28].

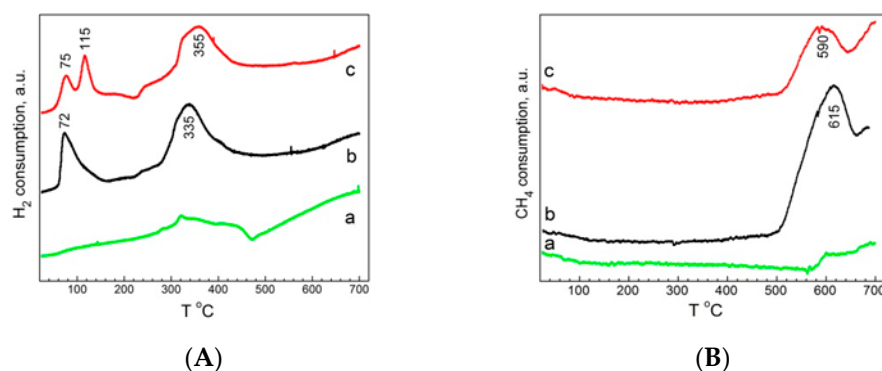


Figure 4. H₂-TPR (A) and CH₄-TPR (B) curves for LMO/Imp (a); Pd-LMO/Imp (b) and Pd-LMO/U-AACVD (c).

In the middle temperature range between 250 and 500 °C, the reduction peak for Pd-LMO/Imp shifts slightly to 335 °C in comparison with that for Pd-LMO/U-AACVD at 355 °C

(Figure 4A). In this case, the consumption of H₂ is due to the reduction of transition metal ions from oxide/perovskite deposited phases. The reduction of powders LaCo_{1-x}Ni_xO₃ and LaCo_{1-x}Fe_xO₃ perovskites were well examined previously [12]. It has been found out that the reduction of LaCo_{1-x}Ni_xO₃ perovskites with H₂ proceeds above 520 °C to Co/Ni metals and La₂O₃ via the formation of intermediate oxygen deficient Brownmillerite-type of phase between 320 °C and 500 °C due to Co³⁺/Ni³⁺ → Co²⁺/Ni²⁺ [12]. The interaction of LaCo_{1-x}Fe_xO₃ with H₂ occurs by reduction of Co³⁺ to Co²⁺ prior to the Fe³⁺ ions [12]. In general, Ni-containing perovskites LaCo_{1-x}Ni_xO₃ are more easily reduced than those containing some Fe, i.e., LaCo_{1-x}Fe_xO₃. In comparison with perovskites, the reduction of Co₃O₄ and Ni_xCo_{3-x}O₄ spinels proceeds between 300 and 400 °C to metals [29]. Based on the redox properties of perovskite and spinel powders, it can be supposed that the consumption of H₂ between 250 and 500 °C is due to the uncompleted reduction of transition metal ions (i.e., Co³⁺ and Ni³⁺ to Co²⁺ and Ni²⁺). The slightly lower reduction temperature observed for Pd-LMO/Imp is related to a higher amount of separate phase of transition metal oxides, that is more easily reduced to metals. The consumption of H₂ by supported catalysts above 580 °C is associated with a complete reduction of transition metal ions to metals by evolving La₂O₃ phase. It should be mentioned that the complete reduction of the supported catalysts starts at higher temperatures in comparison with the powder perovskites [12]. This indicates a possible interaction of transition metal ions with SiO₂-modified alumina support.

Although the strong H₂ reagent allows differentiating the reducibility of supported catalysts with respect to the method of synthesis, the mild CH₄ reagent makes equalizing of the catalysts (Figure 4B). The consumption of CH₄ by supported catalysts starts above 200 °C by developing a reduction peak centered at around 600 °C. It is noticeable that the intensity of this peak is higher for Pd-LMO/Imp. In comparison with Pd-containing catalysts, the supported perovskite LMO/Imp sample that does not contain any Pd exhibits a negligible consumption of CH₄ within this temperature range. The comparison of CH₄-TPR curves of supported catalysts indicates that the peak at around 600 °C can be attributed to the consumption of CH₄ by dispersed PdO-like phase, whose amount is higher in Pd-LMO/Imp. The dispersed PdO-like phase is also responsible for low-temperature consumption of H₂ (Figure 4B).

To analyze the reduction of supported catalysts by CH₄, EPR measurements were undertaken. Figure 5 gives the ex-situ EPR spectra of partially reduced Pd-LMO/Imp sample with CH₄. The EPR spectrum of fresh catalysts displays low intensity signal at $g = 4.28$ due to the impurity Fe³⁺ ions in the alumina support. After the partial reduction of Pd-LMO/Imp sample with CH₄ at 200 °C, the EPR spectrum does not undergo any significant changes. At 500 °C, the reduction of Pd-LMO/Imp with CH₄ results in the appearance of a strong asymmetric signal with an apparent g -value of ≈ 2.17 and line width of 115 mT. The signal intensity increases when the reduction temperature is raised from 500 to 700 °C. The detection of a strong EPR signal for partially reduced catalysts can be related to an appearance of Pd particles due to the consumption of CH₄ by Pd-LMO/Imp sample. To support this supposition, Figure 5 gives also the EPR spectrum of completely reduced Pd-LMO/Imp with H₂ at 700 °C. In this case, the EPR spectrum consists of strong EPR asymmetric signal with an apparent g -factor close to that of CH₄-reduced Pd-LMO/Imp: $g = 2.20$ versus $g = 2.17$, respectively. The important feature of the EPR spectrum of H₂-reduced Pd-LMO/Imp is the strong signal broadening: 145 mT and 115 mT for H₂- and CH₄-reduced Pd-LMO/Imp, respectively. The broadening of the EPR signal after H₂ treatment of Pd-LMO/Imp sample can be associated with a complete reduction at 700 °C of both palladium and transition metal ions to metals, as it was observed by H₂-TPR curves (Figure 4A). In comparison with H₂-reduction, the methane is partially consumed by Pd-LMO/Imp at 700 °C (Figure 4B) as a result of which only the palladium ions are reduced leading to an appearance a narrow EPR signal. The comparative EPR study provides experimental evidence for the reduction of palladium ions during CH₄ treatment of Pd-LMO/Imp at temperatures higher than 200 °C, while transition metal ions to higher extent

remain inactive event at 700 °C. It is of importance that Pd-LMO/U-AACVD reduced with CH₄ at 700 °C displays the same EPR features: there is a strong asymmetric signal with an apparent g -value of =2.17 and line width of 115 mT. The difference comes from the intensities of the signals detected for reduced with CH₄ at 700 °C samples: the normalized intensity is 1.0 for Pd-LMO/Imp versus 0.7 for Pd-LMO/U-AACVD.

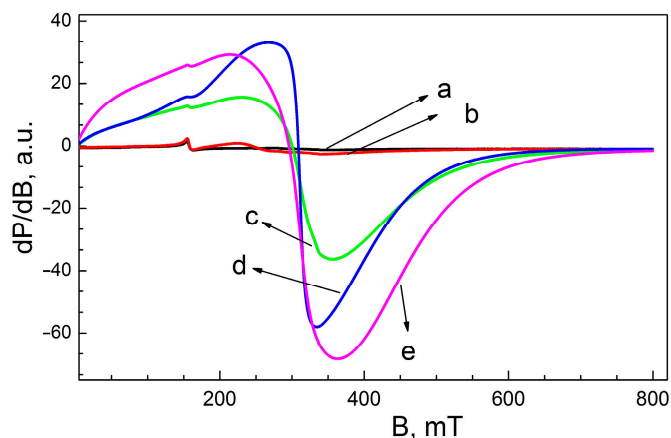


Figure 5. ex-situ EPR spectra of fresh Pd-LMO/Imp (a) and Pd-LMO/Imp reduced with CH₄ at 200 °C (b), 500 °C (c) and 700 °C (d). For the sake of comparison, the completely reduced Pd-LMO/Imp with H₂ at 700 °C is also shown (e).

2.2. Catalytic Activity of Supported Pd-Containing Perovskite over SiO₂-Modified Alumina

2.2.1. Pre-Treatment Tests

In order to compare the reactivity of oxygen species on both catalytic surfaces, experiments on the so-called “depletive” oxidation were performed [30,31]. The test consists of stopping the supply of oxygen in the feed gas mixture after establishing steady-state conditions and monitoring the formation of oxidation products. The duration of “depletive” oxidation experiment was fixed to 70 min, a period within which the emission of oxidation products from both samples was almost completed. The results from “depletive” oxidation of both fresh catalysts are represented in Figure 6.

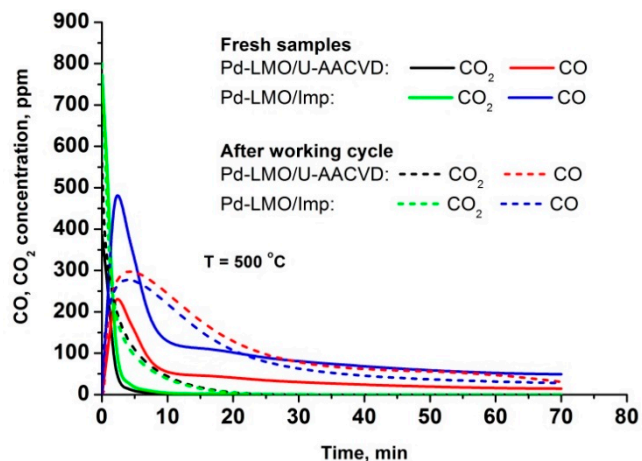


Figure 6. Reductive activation of Pd-LMO/U-AACVD and Pd-LMO/Imp in CH₄/N₂ flow.

The on-line gas-analysis shows that the “depletive” oxidation of both catalysts leads to the formation of CO₂ and CO products. It appears that CO₂ is evolved immediately after the termination of oxygen supply and this process stops within a period of 5–6 min. The CO formation starts only after the CO₂ evolution is ended and it passes through a maximum at about 5–6 min, followed by a slow diminishing for a longer time period. All these observations reveal the redox ability of catalysts that depend on the method of

synthesis. As a measure of redox ability, Table 3 gives the amount of oxygen from catalysts involved in the reaction with CH₄.

Table 3. Amounts of oxygen from the catalysts reacted with methane at 500 °C in CH₄/N₂ flow.

Reacted Oxygen (Uptake)	Fresh Catalyst		After Working Cycle	
	mg O ₂ to CO	mg O ₂ to CO ₂	mg O ₂ to CO	mg O ₂ to CO ₂
Pd-LMO/U-AACVD	1.0	0.4	2.7	0.7
Pd-LMO/Imp	2.6	0.8	2.3	1.0

The quick generation of CO₂ reveals that at 500 °C the methane reduces the catalyst by reaction with surface oxygen species: CH₄ + O_{2,surf(lattice)} → CO₂ + H₂O. At this stage of examination, it is not possible to relate undoubtedly the oxygen species with palladium or transition metal ions. However, the previous data have demonstrated that the PdO supported on γ-Al₂O₃ is reduced with CH₄ to Pd⁰ in the temperature range of 240–290 °C depending on the particle sizes [32], while Co₃O₄ with different morphologies undergoes two steps reduction starting in the temperature range of 540–590 °C [33]. In addition, the ex-situ EPR spectra indicate that the palladium ions are reduced by CH₄ prior to the transition metal ions within the temperature range of 500–700 °C (Figure 4). From the comparative point of view, it is of importance that the process of CO₂ formation is more effective for Pd-LMO/Imp as it was demonstrated by the evaluated amount of O₂ participating in the reaction with CH₄ (Table 3). This is related to different catalyst surface properties: more dispersed PdO phase and higher content of transition metal oxides are established for the catalysts obtained by the impregnation. In comparison with CO₂, the observed continuation of CO formation after the specified test duration is a more complex process and it can be explained either by the reaction of methane with oxygen from the catalyst surface or by the reforming of CH₄ with CO₂ (or H₂O) evolved or by cracking of CH₄ over the metal particles (as it was previously found out for the reduction of Co₃O₄ with CH₄ to CO [33]), but some influence of oxygen traces (10–15 ppm) in the nitrogen gas cannot be excluded. Even in this complex case, the evaluated oxygen amount involved in the reaction with CH₄ to CO is higher for the Pd-LMO/Imp sample. The comparative data of “depletive” oxidation of fresh catalysts evidence clearly that Pd-LMO/Imp contains more mobile oxygen species, which give rise to its higher redox ability.

After the “depletive” oxidation test both samples showed remarkable activation once the oxygen supply was restored. In terms of reaction rate constants (pseudo-first order kinetics), a twofold increase was observed (more specifically k₂/k₁ (500 °C) = 1.85 for Pd-LMO/U-AACVD and 1.90 for Pd-LMO/Imp) after the first cycle. It was reported that after the 110 h of testing in methane combustion over 2% Pd/Al₂O₃ (at 420 °C) the conversion degree decreased from 100% to 88%, but the following treatment in hydrogen (at 200 °C for 1 h) resulted in a restoration of the initial activity [34]. Although the reductive treatment is enhancing the activity of the catalyst, this enhancement is only temporary and it can be lost in oxidizing conditions [35].

2.2.2. Reaction Kinetics

The inlet concentrations of reagents were varied and the corresponding kinetic parameters were calculated by applying the method, described by Duprat [36]. The temperature dependencies of the conversion degree of methane during the reaction of complete oxidation are presented in Figure 7. Details on the calculation procedure were published previously [37,38].

The effect of the external mass transfer limitations was minimized by tests at relatively high values for the hourly space velocity. Preliminary experiments on varying the GHSV_(STP) showed that the reaction rate (calculated by integration alongside the reactor length) increased gradually until we reached 40,000 h⁻¹ and a further increase in the value of the gas film coefficient had no effect on the reaction rate. In addition, calculations on the effect of higher gas velocity at the reactor wall showed a decrease in the conversion within the range of 2–4%, which was compensated during the calculation procedure. Further, in

order to decrease the effect of the internal mass transfer limitations, the catalytic active phase was supported in the form of a thin layer and the values of the effectiveness factor at conversions below 40% were within the range of 0.95–0.99.

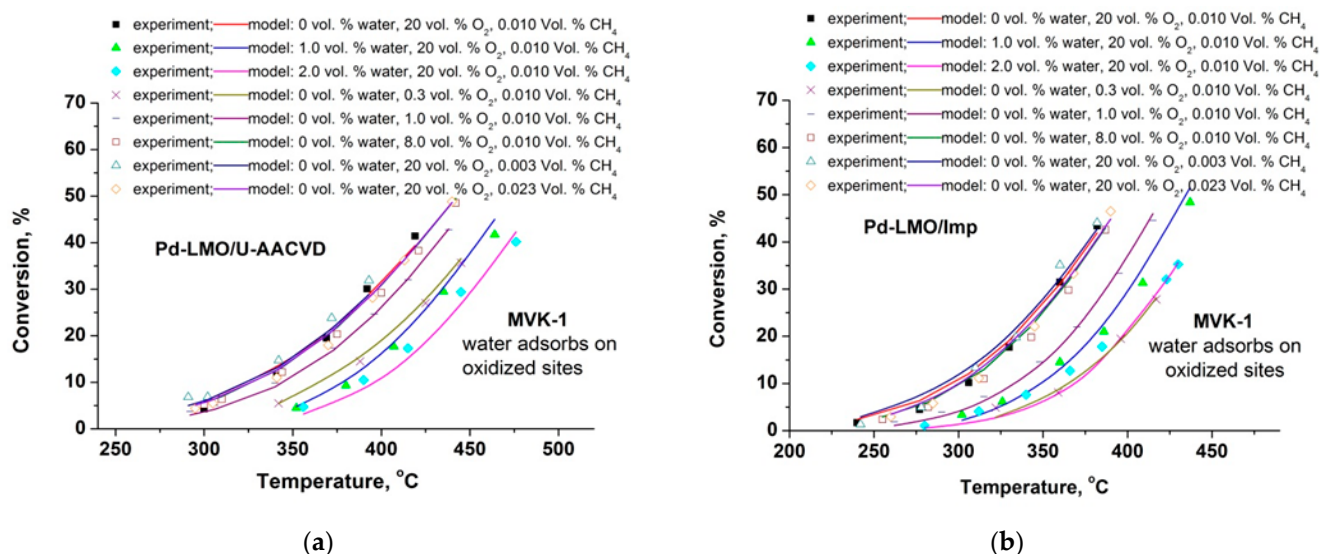


Figure 7. Temperature dependencies of the conversion degree of methane during the reaction of complete oxidation for catalysts obtained by the method of aerosol assisted chemical vapor deposition (U-AACVD) (a) and wet impregnation (Imp) (b)—experimental results and predictions according to the best fitting model—Mars–van Krevelen, where the water molecules compete with the methane molecules for the oxidized active sites.

The applied rate equations contain the following kinetic parameters: pre-exponential coefficient (k_0), reaction orders towards the methane, oxygen and water vapor (m , n , p), the rate constant (k), activation energy (E_a), enthalpy of adsorption (ΔH), and adsorption equilibrium constant (K). The corresponding dimensions for each kinetic parameter and kinetic model are shown below in Tables 4–6. The calculation procedure is based on an integrated computer program where the material balance of the reactor model is solved simultaneously using the suggested multivariate analysis kinetics parameters. The consistency of the obtained results of each run is checked by comparison between the experimental data for the conversion and the predicted values by the model. The applied optimization procedure is based on searching for the lowest value for the squared sum of the residuals (RSS) between the measured conversions and the model predictions, as well as the value of the square correlation coefficient (R^2) within the entire set of varied experimental data.

Based on the experimental results (conversions below 40–45%), an estimation of the kinetic parameters was performed by solving the material balance in an isothermal plug flow type of reactor (PFR) applying a numerical nonlinear optimization procedure, based on iterative reduction of the gradients. The fitting program was applied under different sets of reaction conditions in searching for the global minimum.

As a first approximation a power law kinetic model (PWL) has been applied. The calculated kinetics parameters are represented in Tables 4–6. The parameters calculated based on the power law kinetic model (PWL) suppose almost the same inhibition effect of water vapor on both catalysts. Similar negative reaction orders towards the water were discussed earlier [39]. It should be pointed out that the water vapor is present in all exhaust gas compositions and its impact on the performance of the catalytic converter is very significant.

Table 4. Kinetics parameters based on power-law model.

Model: PWL	Catalyst	k_0	E_a	m (CH ₄)	n (O ₂)	p (H ₂ O)	RSS	R^2
$r = kP_{voc}^m P_{ox}^n P_{water}^p$	Pd-LMO/U-AACVD	68.3	1.36×10^2	0.84	0.18	−0.10	5.4	0.977
	Pd-LMO/Imp	69.2	4.14×10^2	0.90	0.21	−0.11	4.0	0.986

Table 5. Reaction rate expressions and kinetics parameters for applied MVK—models.

Model: MVK-1	Catalyst	$k_{o,ox}$	$E_{a,ox}$	$k_{o,red}$	$E_{a,red}$	$k_{o,water}$	$-\Delta H_{water}$	RSS	R^2
water adsorbs on oxidized sites $r = \frac{k_{red}k_{ox}P_{voc}P}{\gamma k_{red}P_{voc} + k_{ox}P_{ox}(1 + k_{water}P_{water})}$ $\gamma = 2$	Pd-LMO/U-AACVD	1.29×10^4	85.2	1.13×10^2	56.5	4.02×10^3	58.0	2.7	0.988
	Pd-LMO/Imp	2.90×10^4	91.2	2.18×10^2	56.5	6.60×10^3	54.4	3.4	0.980
Model: MVK-2 water adsorbs on reduced sites $r = \frac{k_{red}k_{ox}P_{voc}P_{ox}}{\gamma k_{red}P_{voc}(1 + k_{water}P_{water}) + k_{ox}P_{ox}}$ $\gamma = 2$	Pd-LMO/U-AACVD	8.39×10^2	16.2	3.16×10^2	62.3	5.84×10^3	82.0	4.4	0.980
	Pd-LMO/Imp	2.95×10^2	15.3	1.99×10^3	68.4	6.61×10^3	72.8	4.8	0.983

Table 6. Reaction rate expressions and kinetics parameters for applied Eley—Rideal model.

Model	Catalyst	k_o	E_a	$k_{o,ox}$	$-\Delta H_{ox}$	$k_{o,water}$	$-\Delta H_{water}$	RSS	R^2
ER $r = \frac{kP_{voc}k_{ox}P_{ox}}{1 + k_{ox}P_{ox} + k_{water}P_{water}}$	Pd-LMO/U-AACVD	7.42×10^2	65.9	6.32×10^3	65.5	2.17×10^3	88.4	5.2	0.971
	Pd-LMO/Imp	1.22×10^4	76.9	9.15×10^5	78.0	6.39×10^3	72.5	5.5	0.978

E_{ai} , kJ/mol; k_{oi} , $\text{mol} \cdot \text{s}^{-1} \cdot \text{m}^{-3} \cdot \text{atm}^{-1}$; $k_{oi,pwl}$, $\text{mol} \cdot \text{s}^{-1} \cdot \text{atm}^{-[1 - (m + n + p)]}$; E_{ai} , kJ/mol; ΔH_i , kJ/mol; k_{oi} , atm^{-1} ; $k = k_o \cdot \exp(-E_a/RT)$; $K_{i(voc,ox)} = k_{o,(voc,ox)} \cdot \exp(-\Delta H_{i,voc,ox}/RT)$; $\Delta H_i = E_{ad} - E_{des}$; γ —stoichiometric coefficient for the total combustion reaction (mol O_2 /mol of methane).

In general, the oxi-redox pathway of complete methane oxidation on palladium catalysts proceeds through the dissociation of a methane molecule to form a hydroxyl group and methyl fragment [40,41]. The mechanism of the interaction between the water molecules and the active sites on Pd-containing catalysts is still unclear. A process of slow recombination of hydroxyls (and following water desorption) occurs on the palladium based catalytic surface. It was observed that the isotopic exchange of oxygen with the palladium active centers occurs before desorption of the water [42]. Schwartz et al. [43] reported that catalyst deactivation during methane oxidation can be related to hydroxyl radicals accumulation on the oxide support. The formed hydroxyls affect the oxygen exchange and decrease the Pd catalyst activity [44].

The values of the reaction order with respect to oxygen (ranged at 0.2) suppose that the reaction pathway of oxygen passes through interaction with the catalytic surface (adsorption step with dissociation), which is just the opposite in the case of methane—values approaching unity reveal the possibility of a direct reaction from the gas phase (that is because of the consideration for Eley–Rideal mechanism [45], which is also included). When the oxygen undergoes a dissociative adsorption [$O_2 + 2Z \rightarrow 2Z(O)$], its partial pressure should appear in the rate equation at the power of 1/2 [37,38].

The close values of the apparent activation energies and the reaction orders enable the opportunity to conclude that the reaction mechanism on both catalysts should be the same one and therefore to compare the values of the pre-exponents. Although such an analysis is only tentative, it is obvious that over the Imp sample reaction of complete methane oxidation proceeds with a three times higher rate than on the U-AACVD sample.

Based on the parameters with the PWL model the following mechanistic models were selected for fitting with the experimental results: Mars-van Krevelen (MVK) [46], water molecules compete with the methane molecules for the oxidized or reduced sites; Eley-Rideal (ER) mechanism, water molecules compete with the oxygen for the same type of adsorption sites and methane molecules react directly from the gas phase.

As it can be seen in Tables 4–6, the best fit was obtained with Mars–van Krevelen (MVK-1), where the water molecules compete with the methane molecules for the oxidized adsorption sites. Comparative data on model predicted and experimentally measured conversions are presented in Figure 8.

Calculations show that the rate-determining step (RDS) is the reduction of the active sites, except at low concentration of oxygen (below 1.0 vol.% for Pd-LMO/Imp and 0.3% for Pd-LMO/U-AACVD), where the re-oxidation stage is a more slow process. Despite the relatively higher values for RSS in Table 6, the mechanism of Eley–Rideal, where the methane reacts from the gas phase cannot be completely neglected.

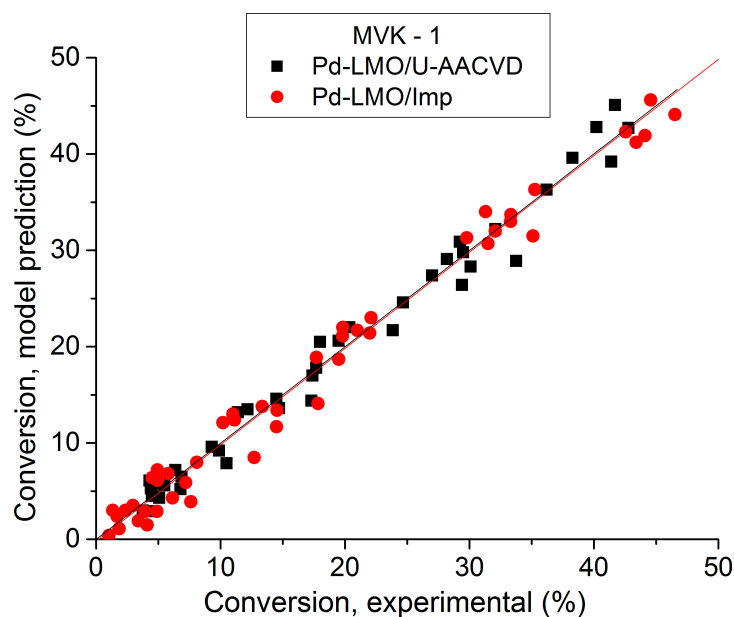


Figure 8. Comparison between the experimentally measured conversions and the predicted by MVK-1 model.

Regarding the thermodynamic consistency of the equilibrium adsorption constants for methane, oxygen and water, the values calculated by the models were constrained within the limits, defined by the guidelines, given by Boudard [47], Vannice et al. [48] and Troops et al. [49]. The following criteria were applied to the calculated values of the enthalpies [49]:

$$-\Delta H_{\text{ads}} > 0 \text{ (} Q_{\text{ads}} > 0\text{)}; 0 < -\Delta S^{\circ}_{\text{ads}} < S^{\circ}_{\text{g}}; 10 \leq -\Delta S^{\circ}_{\text{ads}} \leq 12.2 - 0.0014 \cdot \Delta H_{\text{ads}}$$

where ΔH_{ads} is in kcal/mol, S°_{g} —standard entropy of the gas at 1 atm.

2.3. Ex-Situ XPS Analysis

To understand the observed changes in the catalytic activity of supported catalysts, ex-situ XPS measurements are undertaken. Figures 3 and 9 show the XPS spectra in the Pd 3d and La 3d regions for Pd-LMO/U-AACVD and Pd-LMO/Imp samples. The Pd 3d_{5/2} core level spectra consist of two overlapping high- and low-energy components as in the case of the fresh catalysts (Figure 3). The only parameter that is changed is the ratio between the intensities of the two components: there is a decrease in the intensity of the high-energy components, which is more pronounced for the catalysts obtained by U-AACVD—pyrolysis (Figure 3, Table 1). This means that the highly-oxidized surface Pd^{3+/4+} ions are extracted from the structure of the perovskite-like phase during the catalytic reaction, while Pd²⁺ in PdO phase remains unchanged. The changes in the chemical state are also observed for La (Figure 9).

The typical La 3d core level spectrum displays two separated spin-orbit components (3d_{3/2} and 3d_{5/2}), where each one of them is further on split by multiplet splitting. This is what we observe with the fresh catalysts. The binding energy for La 3d_{5/2} is around 834 eV with energy difference between the 3d_{3/2} and the 3d_{5/2} levels of 17 eV, which correspond to La³⁺ ions. Comparing Pd-LMO/Imp and Pd-LMO/U-AACVD, it appears that the multiplet structure is more well resolved for the Pd-LMO/Imp catalyst, which is related to the slightly different local structure of La in both catalysts: although at Pd-LMO/Imp a mixture of oxides is mainly deposited, Pd-LMO/U-AACVD contains relatively higher amounts of the perovskite phase. After the activity catalytic test, the multiplet splitting becomes less resolved and the 3d_{5/2} level is slightly shifted to 835 eV without changing

the energy difference between the 3d_{3/2} and the 3d_{5/2} levels. This reflects, most probably, the difference in the local structure of La in both the fresh and tested catalysts.

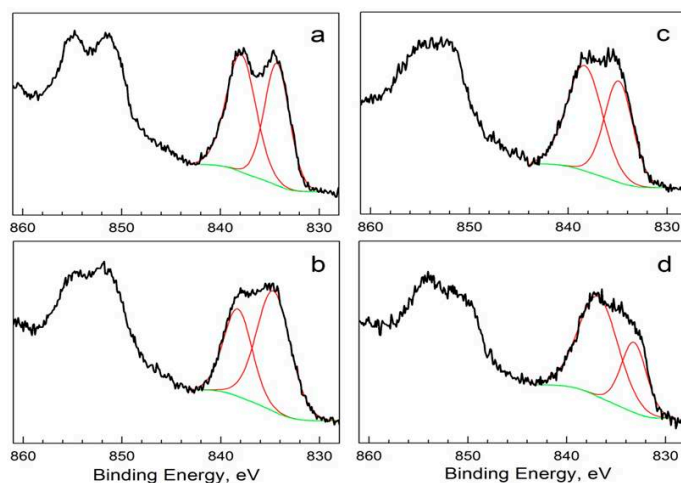


Figure 9. XPS spectra in the La 3d regions for fresh Pd-LMO/Imp (a) and Pd-LMO/U-AACVD (b), as well as for catalytic tested Pd-LMO/Imp (c) and Pd-LMO/U-AACVD (d). The multiplet splitting for La 3d_{5/2} is indicated by red lines.

Furthermore, one can suppose that the different local structures of La can be induced by the extraction of Pd from the perovskite structure during the catalytic reaction. In general, Pd-LMO/U-AACVD undergoes more significant changes under the catalytic activity test due to the extraction of Pd^{3+/4+} ions from the perovskite structure and the formation of PdO-like phase.

This coincides well with the “depletive” oxidation of spent catalysts (Figure 6, Table 3). The formation of CO₂ starts immediately after the stop of O₂ supply as in the case of fresh catalysts, but its formation proceeds in an extended time period (up to 20 min of the experiment, Figure 6). The formation of CO during the interaction of CH₄ with spent catalysts retains its specific features: CO is formed after CO₂ and it is evolved in a longer time period (Figure 6). The comparison between the calculated amounts of oxygen uptake during “depletive” oxidation within the first cycle and the followed “working” cycle treatments show more significant changes within the U-AACVD sample. More specifically, there is a remarkable increase in the amount of oxygen capable to convert methane to CO and CO₂ (an increase of the order of 2–3 times), while the changes with the Pd-LMO/Imp sample are in the margin of the experimental error. It is worth mentioning that the amounts of oxygen species involved in the CH₄ reaction become nearly the same for both supported catalysts. This result supports once again the XPS data on the extraction of Pd^{3+/4+} ions from the perovskite structure concomitant with the formation of PdO-like phase over Pd-LMO/U-AACVD surface during the catalytic test (Figure 9).

According to the CH₄-TPR data for both catalysts, the process of oxygen consumption begins at temperatures above 200 °C and proceeds with a very high rate at temperatures above 500 °C. Therefore one could suppose that at the temperature range of 200–500 °C the methane from gas phase reacts with the lattice oxygen with higher reactivity (thus producing CO₂ mainly), while at higher temperatures a process of incomplete oxidation of CH₄ to CO occurs. The highly reactive lattice oxygen is most probably associated with palladium ions from dispersed PdO-like phase, while oxygen species bonded to transition metal ions from other oxide phases are not enough reactive to convert methane to CO₂ (and H₂O). However, their role could be related to the oxygen supply to Pd—active sites during the methane oxidation. Supporting this statement, the H₂-TPR curves revealed the different reducibility of transition metal ions depending on the method of synthesis: the reduction peak for Pd-LMO/Imp at 335 °C is shifted with 20 °C to the lower temperatures in comparison with Pd-LMO/U-AACVD (Figure 4A). This indicates an occurrence of more mobile oxygen species linked to transition metal ions for Pd-LMO/Imp. These

oxygen species are able to restore the oxygen vacancies after methane reaction with the Pd-bonded oxygen.

Due to the well dispersed PdO-like phase and of oxygen storage capability of transition metal ions, Pd-LMO/Imp sample displays a better catalytic performance. Catalytic activity tests under the basic conditions (20% oxygen, absence of an additional amount to that originated from the reaction water vapor) demonstrate that the light-off temperature (T50) for Pd-LMO/Imp is lower with about 44 °C in comparison with that of Pd-LMO/U-AACVD (T50 is at 436 °C). The so proposed scheme of participation of oxygen species in CH₄ oxidation is in agreement with Mars–van Krevelen mechanism: adsorbed CH₄ reacts with lattice oxygen species leading to a formation of adsorbed products such as CO₂ and H₂O concomitant with the creation of oxygen vacancies. The next step is associated with desorption of CO₂ and H₂O molecules together with regeneration of lattice oxygen species by refilling of oxygen vacancies. The intimate contact between PdO-like phase and transition metal oxides favors the oxygen exchange between them (see also Figure 2b).

In comparison with Pd-LMO/Imp, the Pd-LMO/U-AACVD sample contains relatively higher amounts of the perovskite phase and it undergoes a significant change after the catalytic reaction due to the extraction of Pd from the perovskite structure during the catalytic reaction. As it was reported [15], a significant improvement in the oxidation activity of the materials was observed when the noble metal is not completely reintegrated into the perovskite crystal. Supports that possess high oxygen mobility can behave as oxygen suppliers to the Pd—active sites [42,50]. As it was reported earlier, the Co²⁺ ions can be active sites for dissociative adsorption of oxygen molecules thus forming activated oxygen species [51].

2.4. Preliminary Data on Possible Practical Application

The thermal stability of supported catalysts was examined in order to test their potential practical applicability. The results show that the catalyst exhibited higher activity (Imp) was examined by aging treatment at 505 °C for 120 h in air, containing 1.2 vol.% water vapor. The tests result showed an increase in T50 with 5 °C, which difference is in the experimental error margin and therefore it can be considered as promising regarding the possible practical application of the synthesized material.

On the basis of the results from tests with a fixed bed reactor a metal monolithic substrate was examined for possible practical application in the development of an industrial catalyst for methane combustion by assembling it with the synthesized Pd-containing perovskite active phase. The catalytic support has been obtained by using of VDM[®] Aluchrom Y Hf foil (ferritic chrome steel alloyed with yttrium and hafnium, thickness 0.20 mm), thermally treated in air at 925 °C and rolled to create tubes with circular cross-section with length of 110 mm and diameter of 3.5 mm so representing the geometrical configuration of a single monolithic channel. Experimental data from the catalytic tests with the monolithic sample, prepared on the basis on the wet impregnated sample (Pd-LMO/Imp/Aluchrom) were used for model calculations, performed by using of a two-dimensional heterogeneous model for monolithic reactor, accounting for both external and internal mass transfer effects. The main principles of the applied model are published by Belfiore [52]. Finite difference method was used and the computation code was written in standard Excel[®] (Microsoft) program. Figure 10a shows the results from experiments with the monolithic element. The model calculations on the needed amount of catalyst for achieving a specified degree of waste gases purification (for example if 98% of the methane is to be combusted in humid air at adiabatic conditions (Figure 10b,c).

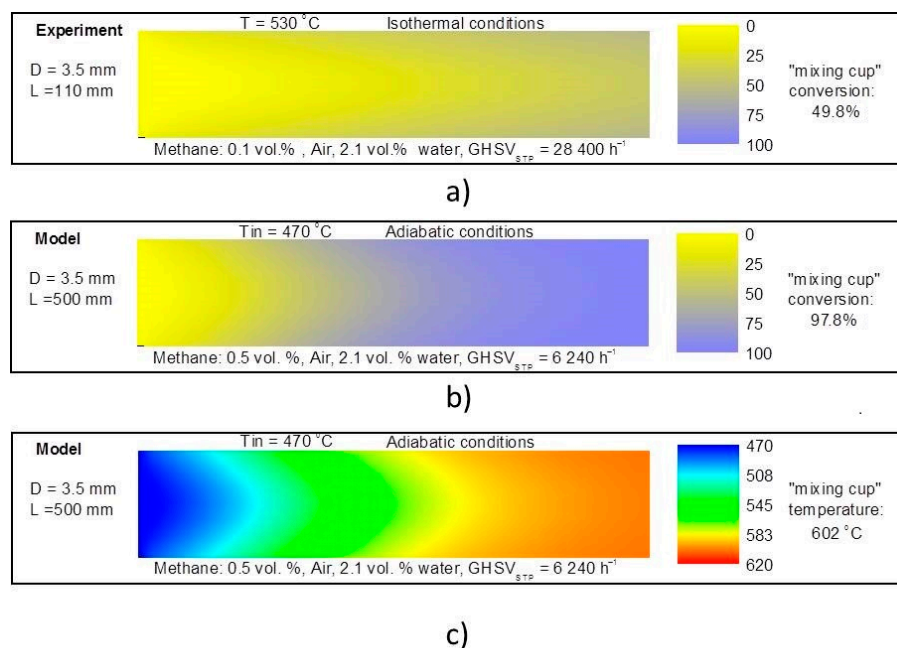


Figure 10. Experimental data on the activity of Pd-LMO/Imp/Aluchrom at isothermal conditions (a) and calculation of catalyst amount needed for 98.0% purification of waste gas (air) containing methane in presence of water vapor at adiabatic conditions (b,c).

Due to the adiabatic effect of the reaction (inlet concentration of methane 0.5 vol.% methane), the temperature at the outlet of the reactor increased by $132\text{ }^{\circ}\text{C}$. The numerical investigation showed that the desired conversion of 98% can be realized when the length of the monolithic element is about 4.5 times longer than the used for the described above laboratory experiments.

3. Experimental

3.1. Catalyst Preparation

The modification of γ -alumina with SiO_2 is accomplished by impregnation with silica sol (colloidal silica, 40% water solution). The alumina particle sizes varied between 0.5 and 0.8 μm . The content of SiO_2 with respect to γ -alumina equals 2 wt. %. The SiO_2 -modified/ γ -alumina is used as a support for catalytic phase deposition.

The first method of active phase deposition consists in conventional wet impregnation of SiO_2 -modified/ γ -alumina with a citrate solution containing all metal ions (La, Co, Ni, Fe and Pd). The citrate solution is prepared by adding reagents $\text{La}(\text{NO}_3)_3 \cdot 6\text{H}_2\text{O}$, CoCO_3 , NiCO_3 , $\text{Fe}(\text{NO}_3)_3 \cdot x\text{H}_2\text{O}$ and $\text{Pd}(\text{NO}_3)_2 \cdot x\text{H}_2\text{O}$ to an aqueous solution of citric acid (0.1 M). The Pd loading is 15%, while the nominal perovskite composition is $\text{La}(\text{Co}_{0.8}\text{Ni}_{0.1}\text{Fe}_{0.1})_{0.85}\text{Pd}_{0.15}\text{O}_3$. A clear solution with a concentration of 0.5 M in regard to La is obtained after stirring at $60\text{ }^{\circ}\text{C}$, then the solution is cooled down to room temperature. The impregnated support was heated at $400\text{ }^{\circ}\text{C}$ for 3 h in air in order to decompose the citrate salts, and then the obtained solid residue was annealed at $600\text{ }^{\circ}\text{C}$ for 3 h in air. The temperature treatment procedure is suitable for the preparation of substituted perovskites with high specific surface area, as was previously shown [13]. The weight amount of the deposited perovskite is 10%. In addition, the impregnation method is also used for the preparation of Pd-free perovskite $\text{LaCo}_{0.8}\text{Ni}_{0.1}\text{Fe}_{0.1}\text{O}_3$, supported on SiO_2 -modified/ γ -alumina.

The second method of active phase deposition is based on the aerosol assisted chemical vapor deposition (AACVD) [53,54] with ultrasonic vaporization at atmospheric pressure [55]. The reaction between the reactant in the gas phase and the alumina support was intensified by pyrolysis at maintaining conditions close to isothermal ($400\text{ }^{\circ}\text{C}$) by operation in a drilled large metal block (Al-alloy). In order to compare the supported catalysts obtained by two preparation methods, the same citric solution of La, Co, Ni, Fe and Pd ions is used. The final heat treatment is also accomplished at $600\text{ }^{\circ}\text{C}$ for 3 h.

For the sake of convenience, the supported catalysts obtained by two methods will be further on denoted as Pd-LMO/Imp and Pd-LMO/U-AACVD, respectively. The Pd-free perovskite $\text{LaCo}_{0.8}\text{Ni}_{0.1}\text{Fe}_{0.1}\text{O}_3$ supported on SiO_2 -modified/ γ -alumina is indicated by LMO/Imp.

3.2. Catalyst Characterization

The powder X-ray structural analysis was conducted on a Bruker Advance 8 diffractometer with a LynxEye detector ($\text{CuK}\alpha$ radiation). All XRD patterns were recorded at 0.02° 2θ steps of 2 s duration. The computer program WinPLOTR was used for XRD patterns calculation with the pseudo-Voigt function applied to model the peak shape.

The morphologies of catalyst surfaces were observed using a JEOL JSM-5510 scanning electron microscope. The elemental composition of the precursors and target phospholivines was determined by energy dispersive X-ray spectroscopy (EDS) using a JSM 6390 scanning electron microscope and an INCA Oxford EDS detector.

The TEM investigations were performed on a TEM JEOL 2100 instrument at accelerating voltage of 200 kV. The specimens were prepared by grinding and dispersing them in ethanol by ultrasonic treatment for 6 min. The suspensions were dripped on standard holey carbon/Cu grids. The TEM micrographs were made using digital image analysis of reciprocal space parameters. The analysis was carried out by the Digital Micrograph software.

The porous texture of the samples was examined by low-temperature (77.4 K) nitrogen adsorption using Quantachrome (Boynton Beach, FL, USA) NOVA 1200e instrument. The specific surface area was evaluated by the BET method at a relative pressure p/p_0 within the range of 0.10–0.30. The total pore volume is calculated by the Barrett–Joyner–Halenda method.

The XPS study was carried out using an ESCALAB MkII (VG Scientific, East Grinstead, UK) electron spectrometer at a base pressure in the analysis chamber of 5×10^{-10} mbar (during the measurement 1×10^{-8} mbar), using a Mg $\text{K}\alpha$ X-ray source (excitation energy $h\nu = 1253.6$ eV) and an Al $\text{K}\alpha$ X-ray source (excitation energy $h\nu = 1486.6$ eV). The instrumental resolution measured as the full width at the half-maximum (FWHM) of the Ag 3d_{5/2} photoelectron peak is about 1 eV. The energy scale is corrected with respect to the C 1s peak maximum at 285 eV for electrostatic charging. The fitting of the recorded XPS spectra was performed, using a symmetrical Gaussian–Lorentzian curve fitting after Shirley's type of subtraction of the background.

The EPR spectra in the form of a first derivative of the absorption signal was detected by a Bruker EMX^{plus} EPR spectrometer operating in the X-band (9.4 GHz) within the temperature range of 100–500 K. The powdered samples were homogenized and dried at 100 °C before every experiment. The amount of each measurable sample was about 30–40 mg.

Temperature programmed reduction (TPR) experiments were carried out in the measurement cell of a differential scanning calorimeter (DSC), model DSC-111 (SETARAM), directly connected to a gas chromatograph (GC), within the 300–973K range at a 10 K/min heating rate in a flow of $\text{Ar:H}_2 = 9:1$ or $\text{He:CH}_4 = 9:1$, the total flowrate being 20 mL/min. A cooling trap between DSC and GC removed the water and CO_2 obtained during the reduction. To perform the ex-situ EPR measurements of the partially reduced oxides, the reduction process was interrupted at selected temperatures and then the samples were cooled down to room temperature in an Ar:H_2 or He:CH_4 flow followed by Ar treatment for 10 min.

3.3. Catalytic Activity Measurements

The catalytic activity tests were carried out in a continuous-flow type of reactor and the following testing conditions were applied: catalyst bed volume of 0.5 cm^3 , irregularly shaped particles with an average size of 0.65 mm (fraction of 0.5–0.8 mm), reactor diameter of 7.0 mm, gaseous hourly space velocity (GHSV) of $120,000 \text{ h}^{-1}$. The effects of the internal diffusion limitations were neglected as the particles of γ -alumina were supported by a thin

layer with a thickness of 20–30 μm and results up to conversion degree of about 40% were used for reaction rate calculations. The characteristics of the catalyst bed correspond to a chain of more than 10 ideal-mixing cells along the reactor axis and therefore the flow conditions can be considered to be close to the behavior of an isothermal plug flow reactor (PFR). The inlet concentrations were varied as follows: methane feed concentrations were set at levels of 0.003, 0.010 and 0.023 vol.%, oxygen at levels of 0.3, 1.0, 8.0 and 20.0 vol.%, water vapour at levels of 0, 1.0 and 2.0 vol.%. All gas mixtures were balanced to 100% with nitrogen (4.0). The reproducibility of the measured conversion degrees was established by repeating the tests under identical conditions and the calculated value for the standard deviation ($\pm 1.75\%$) was taken from the average values from six measurements. The gas analysis was performed using the mass-spectrometer of the CATLAB (Hiden Analytical, Warrington, UK) system and in addition to it the on-line gas-analyzers of CO/CO₂/O₂ (Maihak, Hamburg, Germany) and THC-FID (total hydrocarbon content with a flame ionization detector, Horiba, Kyoto, Japan). The catalysts after the catalytic test are subjected to ex-situ XPS analysis.

4. Conclusions

The wet impregnation and the aerosol assisted chemical vapor deposition are effective chemical techniques for the preparation of supported catalysts for CH₄ combustion. The impregnation of SiO₂-modified/ γ -alumina support with citrate solutions of La, Co, Ni, Fe and Pd leads to a deposition of an intimate mixture of well dispersed PdO-like phase, transition metal oxides and Pd-containing perovskite on the support surface, while the aerosol assisted chemical vapor deposition of the same citrate solution yields a Pd-containing perovskite phase as the main product. The occurrence of dispersed PdO-like phase determines the higher redox ability of catalysts obtained by the impregnation method—the catalyst obtained by impregnation method contains mobile oxygen species in higher content in comparison with that obtained by modified chemical vapor deposition.

The observed better catalytic performance of Pd-LMO/Imp can be attributed to the appearance of well dispersed PdO-like phase, as well as to the higher oxygen storage capability of transition metal ions. The catalyst Pd-LMO/U-AACVD contains relatively higher amounts of the perovskite phase and it undergoes a significant change after the catalytic reaction due to the extraction of Pd from the perovskite structure.

Based on the results from the kinetic models fitting, the reaction pathway over both Pd-LMO/Imp and Pd-LMO/U-AACVD catalysts proceeds most probably through Mars–van Krevelen mechanism (lowest values for RSS, Table 5). The intimate contact between PdO-like phase and transition metal oxides favors the oxygen mobility. The inhibiting effect of water molecules is due to the competition with the oxygen molecules for chemisorption on the oxidized active sites. In addition, the mechanism of Eley–Rideal, where the methane molecules react from gas phase cannot be completely neglected.

The tests results on a hydrothermally aged catalyst that showed higher initial activity (Imp) reveal noticeably weak deactivation, which result can be considered as promising regarding the possible practical application of the synthesized material. The established correlations between synthesis history, structure and morphology of catalysts and their catalytic activity are of significance in order to design more effective monolith catalysts for the reaction of methane combustion at low temperatures.

Preliminary data on the practical applicability of the La(Co_{0.8}Ni_{0.1}Fe_{0.1})_{0.85}Pd_{0.15}O₃—based catalyst, supported on monolithic substrate VDM[®] Aluchrom Y Hf are obtained. Taking into account the overall high thermal stability of the active phase and the carrier, one may conclude that the prepared catalyst could contribute to response the currently growing demands aimed at reducing methane emissions. Therefore, future research will focus on further optimizing the active phase composition in order to attain high sulfur resistance and new monolithic substrates such as mullite and various shaped stainless steels should be investigated for their resistance to alkali metal oxides (as present in some flue gases).

Author Contributions: Conceptualization, A.N., R.S., E.Z.; Methodology, S.S., E.Z., A.N., R.S.; Validation, S.S., G.I., S.H., K.T.; Investigation, S.S., G.I., K.T., S.H.; Resources, A.N., R.S., Data curation, S.S., G.I.; Writing—original draft preparation, A.N., E.Z., R.S.; Writing—review and editing, S.S., A.N., R.S., E.Z.; Visualization, S.S., G.I., S.H., K.T., E.Z., A.N., R.S.; Supervision, E.Z., R.S.; Project administration, A.N.; Funding acquisition, A.N. All authors have read and agreed to the published version of the manuscript.

Funding: Research equipment of distributed research infrastructure INFRAMAT ДЮ1- 382/18.12.2020 (part of Bulgarian National roadmap for research infrastructures) supported by Bulgarian Ministry of Education and Science was used in this investigation. The authors thank the National Science Fund of Bulgaria for the financial support under the Contract KII-06-H49/4.

Institutional Review Board Statement: Not applicable.

Informed Consent Statement: Not applicable.

Data Availability Statement: The data presented in this study are available on request from the corresponding author.

Conflicts of Interest: The authors declare no conflict of interest.

References

1. Federal Register/Vol. 78, No. 63/Tuesday, April 2, 2013/Proposed Rules, Environmental Protection Agency, 40 CFR Part 98, 2013 Revisions to the Greenhouse Gas Reporting Rule and Proposed Confidentiality Determinations for New or Substantially Revised Data Elements. Available online: <https://www.govinfo.gov/content/pkg/FR-2013-04-02/pdf/2013-06093.pdf> (accessed on 2 April 2013).
2. European Commission Global Methane Reduction Actions, Ref. Ares (2013) 2843722-06/08/2013. Available online: https://www.globalmethane.org/documents/EC_GMI_reduction_actions.pdf (accessed on 6 August 2013).
3. Bordelanne, O.; Montero, M.; Bravin, F.; Prieur-Vernat, A.; Oliveti-Selmi, O.; Pierre, H.; Papadopoulo, M.; Muller, T. Biomethane CNG hybrid: A reduction by more than 80% of the greenhouse gases emissions compared to gasoline. *J. Nat. Gas Sci. Eng.* **2011**, *3*, 617–624. [CrossRef]
4. Machin, N.E.; Cakırca, E.E.; Ates, A. Catalytic combustion of methane. In Proceedings of the 6th International Advanced Technologies Symposium (IATS'11), Elazığ, Turkey, 16–18 May 2011; pp. 253–256.
5. Hurtado, P.; Ordycey, S.; Sastre, H.; Diez, F.V. Combustion of methane over palladium catalyst in the presence of inorganic compounds: Inhibition and deactivation phenomena. *Appl. Catal. B Environ.* **2004**, *47*, 85–93. [CrossRef]
6. Ersson, A. Materials for High-Temperature Catalytic Combustion. Ph.D. Thesis, Kungliga Tekniska Högskolan Department of Chemical Engineering and Technology Chemical Technology, Stockholm, Sweden, 2003.
7. Cimino, S.; Lisi, L.; Pirone, R.; Russo, G.; Turco, M. Methane combustion on perovskites-based structured catalysts. *Catal. Today* **2000**, *59*, 19–31. [CrossRef]
8. Barbato, P.S.; Di Sarli, V.; Landi, G.; Di Benedetto, A. High pressure methane catalytic combustion over novel partially coated LaMnO₃-based monoliths. *Chem. Eng. J.* **2015**, *259*, 381–390. [CrossRef]
9. Di Sarli, V.; Barbato, P.S.; Benedetto, A.D.; Landi, G. Start-up behavior of a LaMnO₃ partially coated monolithic combustor at high pressure. *Catal. Today* **2015**, *242*, 200–210. [CrossRef]
10. Zhu, H.; Zhang, P.; Dai, S. Recent Advances of Lanthanum-Based Perovskite Oxides for Catalysis. *ACS Catal.* **2015**, *5*, 6370–6385. [CrossRef]
11. Wang, Y.; Ren, J.; Wang, Y.; Zhang, F.; Liu, X.; Guo, Y.; Lu, G. Nanocasted Synthesis of Mesoporous LaCoO₃ Perovskite with Extremely High Surface Area and Excellent Activity in Methane Combustion. *J. Phys. Chem. C* **2008**, *112*, 15293–15298. [CrossRef]
12. Ivanova, S.; Senyshyn, A.; Zhecheva, E.; Tenchev, K.; Stoyanova, R.; Fuess, H. Crystal structure, microstructure and reducibility of LaNi_xCo_{1-x}O₃ and LaFe_xCo_{1-x}O₃ Perovskites (0 < x ≤ 0.5). *J. Solid State Chem.* **2010**, *183*, 940–950. [CrossRef]
13. Stanchovska, S.; Zhecheva, E.; Stoyanova, R.; Naydenov, A. Preparation and characterization of palladium containing nickel-iron-cobalt perovskite catalysts for complete oxidation of propane. *Bulg. Chem. Commun.* **2017**, *49*, 107–113.
14. Stanchovska, S.; Markov, P.; Tenchev, K.; Stoyanova, R.; Zhecheva, E.; Naydenov, A. Preparation and characterization of palladium containing nickel-iron-cobalt perovskite catalysts for the complete oxidation of C1–C6 alkanes. *React. Kinet. Mech. Catal.* **2017**, *122*, 931–942. [CrossRef]
15. Eyssler, A.; Winkler, A.; Safonova, O.; Nachtegal, M.; Matam, S.K.; Hug, P.; Weidenkaff, A.; Ferri, D. On the State of Pd in Perovskite-Type Oxidation Catalysts of Composition A(B,Pd)O_{3±δ} (A = La, Y; B = Mn, Fe, Co). *Chem. Mater.* **2012**, *24*, 1864–1875. [CrossRef]
16. Nishihata, Y.; Mizuki, J.; Akao, T.; Tanaka, H.; Uenishi, M.; Kimura, M.; Okamoto, T.; Hamada, N. Self-regeneration of a Pd-perovskite catalyst for automotive emissions control. *Nature* **2002**, *418*, 164. [CrossRef]

17. Uenishi, M.; Taniguchi, M.; Tanaka, H.; Kimura, M.; Nishihata, Y.; Mizuki, J.; Kobayashi, T. Redox behavior of palladium at start-up in the Perovskite-type LaFePdO_x automotive catalysts showing a self-regenerative function. *Appl. Catal. B* **2005**, *57*, 267–273. [[CrossRef](#)]
18. Uenishi, M.; Tanaka, H.; Taniguchi, M.; Tan, I.; Sakamoto, Y.; Matsunaga, S.; Yokota, K.; Kobayashi, T. The reducing capability of palladium segregated from perovskite-type LaFePdO_x automotive catalysts. *Appl. Catal. A* **2005**, *296*, 114–119. [[CrossRef](#)]
19. Tanaka, H.; Taniguchi, M.; Kajita, N.; Uenishi, M.; Tan, I.; Sato, N.; Narita, K.; Kimura, M. Design of the intelligent catalyst for Japan ULEV standard. *Top. Catal.* **2004**, *30*, 389–396. [[CrossRef](#)]
20. Tanaka, H.; Taniguchi, M.; Uenishi, M.; Kajita, N.; Tan, I.; Nishihata, Y.; Mizuki, J.; Narita, K.; Kimura, M.; Kaneko, K. Self-Regenerating Rh- and Pt-Based Perovskite Catalysts for Automotive-Emissions Control. *Angew. Chem. Int. Ed.* **2006**, *45*, 5998–6002. [[CrossRef](#)]
21. Dacquin, J.P.; Cabiñ, M.; Henry, C.R.; Lancelot, C.; Dujardin, C.; Raouf, S.R.; Granger, P. Structural changes of nano-Pt particles during thermal ageing: Support-induced effect and related impact on the catalytic performances. *J. Catal.* **2010**, *270*, 299–309. [[CrossRef](#)]
22. Dacquin, J.P.; Lancelot, C.; Dujardin, C.; Cordier-Robert, C.; Granger, P. Support-Induced Effects of LaFeO₃ Perovskite on the Catalytic Performances of Supported Pt Catalysts in DeNO_x Applications. *J. Phys. Chem. C* **2011**, *115*, 1911–1921. [[CrossRef](#)]
23. Wenge, L.; Deyong, G.; Xin, X. Research Progress of Palladium Catalysts for Methane Combustion. *China Pet. Proc. Petrochem. Techn. Rev.* **2012**, *14*, 1–9.
24. Zasada, F.; Janas, J.; Piskorz, W.; Gorczynska, M.; Sojka, Z. Total Oxidation of Lean Methane over Cobalt Spinel Nanocubes Controlled by the Self-Adjusted Redox State of the Catalyst: Experimental and Theoretical Account for Interplay between the Langmuir–Hinshelwood and Mars–Van Krevelen Mechanisms. *ACS Catal.* **2017**, *7*, 2853–2867. [[CrossRef](#)]
25. Meille, V. Review on methods to deposit catalysts on structured surfaces. *Appl. Catal. A* **2006**, *315*, 1–17. [[CrossRef](#)]
26. Keav, S.; Matam, S.K.; Ferri, D.; Weidenkaff, A. Structured Perovskite-Based Catalysts and Their Application as Three-Way Catalytic Converters—A Review. *Catalysts* **2014**, *4*, 226–255. [[CrossRef](#)]
27. Eyssler, A.; Mandaliev, P.; Winkler, A.; Hug, P.; Safonova, O.; Figi, R.; Weidenkaff, A.; Ferri, D. The Effect of the State of Pd on Methane Combustion in Pd-Doped LaFeO₃. *J. Phys. Chem. C* **2010**, *114*, 4584–4594. [[CrossRef](#)]
28. Zhou, R.; Zhao, B.; Yue, B. Effects of CeO₂–ZrO₂ present in Pd/Al₂O₃ catalysts on the redox behavior of PdO_x and their combustion activity. *Appl. Surface Sci.* **2008**, *254*, 4701–4707. [[CrossRef](#)]
29. Lim, T.H.; Cho, S.J.; Yang, H.S.; Engelhard, M.H.; Kim, D.H. Effect of Co/Ni ratios in cobalt nickel mixed oxide catalysts on methane combustion. *Appl. Catal. A* **2015**, *505*, 62–69. [[CrossRef](#)]
30. Books, C.S. The kinetics of hydrogen and carbon monoxide oxidation over a manganese oxide. *J. Catal.* **1967**, *8*, 272–282. [[CrossRef](#)]
31. Santos, V.P.; Pereira, M.F.R.; Yrffo, J.J.M.; Figueiredo, J.L. The role of lattice oxygen on the activity of manganese oxides towards the oxidation of volatile organic compounds. *Appl. Catal. B* **2010**, *99*, 353–363. [[CrossRef](#)]
32. Baylet, A.; Maricot, P.; Duprez, D.; Castellazzi, P.; Groppi, G.; Forzatti, P. In situ Raman and in situ XRD analysis of PdO reduction and Pd⁰ oxidation supported on γ-Al₂O₃ catalyst under different atmospheres. *Phys. Chem. Chem. Phys.* **2011**, *13*, 4607–4613. [[CrossRef](#)]
33. Chen, Z.; Wang, S.; Liu, W.; Gao, X.; Gao, D.; Wang, M.; Wang, S. Morphology-dependent performance of Co₃O₄ via facile and controllable synthesis for methane combustion. *Appl. Catal. A Gen.* **2016**, *525*, 94–102. [[CrossRef](#)]
34. Kucharczyk, B. Activity of monolithic Pd/Al₂O₃ catalysts in the combustion of mine ventilation air methane. *Pol. J. Chem. Technol.* **2011**, *13*, 57–62. [[CrossRef](#)]
35. Abbasi, R.; Huang, G.; Istratescu, G.M.; Wu, L.; Hayes, R.E. Methane oxidation over Pt, Pt/Pd, and Pd based catalysts: Effects of pre-treatment. *Can. J. Chem. Eng.* **2015**, *93*, 1474–1482. [[CrossRef](#)]
36. Duprat, F. Light-off curve of catalytic reaction and kinetics. *Chem. Eng. Sci.* **2002**, *57*, 901–911. [[CrossRef](#)]
37. Todorova, S.; Naydenov, A.; Kolev, H.; Holgado, J.P.; Ivanov, G.; Kadinov, G.; Caballero, A. Mechanism of complete *n*-hexane oxidation on silica supported cobalt and manganese catalysts. *Appl. Catal. A* **2012**, *413–414*, 43–51. [[CrossRef](#)]
38. Markova-Velichkova, M.; Lazarova, T.; Tumbalev, V.; Ivanov, G.; Kovacheva, D.; Stefanov, P.; Naydenov, A. Complete oxidation of hydrocarbons on YFeO₃ and LaFeO₃ catalysts. *Chem. Eng. J.* **2013**, *231*, 236–244. [[CrossRef](#)]
39. Gholami, R.; Alyani, M.; Smith, K.J. Deactivation of Pd Catalysts by Water during Low Temperature Methane Oxidation Relevant to Natural Gas Vehicle Converters. *Catalysts* **2015**, *5*, 561–594. [[CrossRef](#)]
40. Fujimoto, K.; Ribeiro, F.H.; Avalos-Borja, M.; Iglesia, E. Structure and Reactivity of PdO_x/ZrO₂ Catalysts for Methane Oxidation at Low Temperatures. *J. Catal.* **1998**, *179*, 431–442. [[CrossRef](#)]
41. Chin, Y.; Iglesia, E. Elementary Steps, the Role of Chemisorbed Oxygen, and the Effects of Cluster Size in Catalytic CH₄–O₂ Reactions on Palladium. *J. Phys. Chem. C* **2011**, *115*, 17845–17855. [[CrossRef](#)]
42. Ciuparu, D.; Pfefferle, L. Contributions of lattice oxygen to the overall oxygen balance during methane combustion over PdO-based catalysts. *Catal. Today* **2002**, *77*, 167–179. [[CrossRef](#)]
43. Schwartz, W.R.; Ciuparu, D.; Pfefferle, L.D. Combustion of Methane over Palladium-Based Catalysts: Catalytic Deactivation and Role of the Support. *J. Phys. Chem. C* **2012**, *116*, 8587–8593. [[CrossRef](#)]
44. Schwartz, W.R.; Pfefferle, L.D. Combustion of Methane over Palladium-Based Catalysts: Support Interactions. *J. Phys. Chem. C* **2012**, *116*, 8571–8578. [[CrossRef](#)]

45. Vannice, M.A. *Kinetics of Catalytic Reactions*; Springer Science-Business Media, Inc.: New York, NY, USA, 2005.
46. Mars, P.; van Krevelen, D.W. Oxidations carried out by means of vanadium oxide catalysts. *Chem. Eng. Sci.* **1954**, *3*, 41–59. [[CrossRef](#)]
47. Boudart, M. Two-step catalytic reactions. *AIChE J.* **1972**, *18*, 465–478. [[CrossRef](#)]
48. Vannice, M.A.; Hyun, S.H.; Kalpakci, B.; Liauh, W.C. Entropies of adsorption in heterogeneous catalytic reactions. *J. Catal.* **1979**, *56*, 358–362. [[CrossRef](#)]
49. Toops, T.J.; Walters, A.B.; Vannice, M.A. Methane combustion over La₂O₃-based catalysts and γ -Al₂O₃. *Appl. Catal. A: Gen.* **2002**, *233*, 125–140. [[CrossRef](#)]
50. Ciuparu, D.; Perkins, E.; Pfefferle, L. In situ DR-FTIR investigation of surface hydroxyls on γ -Al₂O₃ supported PdO catalysts during methane combustion. *Appl. Catal. A Gen.* **2004**, *263*, 145–153. [[CrossRef](#)]
51. Łojewska, J.; Kołodziej, A.; Żak, J.; Stoch, J. Pd/Pt promoted Co₃O₄ catalysts for VOCs combustion: Preparation of active catalyst on metallic carrier. *Catal. Today* **2005**, *105*, 655–661. [[CrossRef](#)]
52. Belfiore, L.A. *Transport Phenomena for Chemical Reactor Design*; John Wiley & Sons, Inc.: Hoboken, NJ, USA, 2003.
53. Marchand, P.; Hassan, I.A.; Parkin, I.P.; Carmalt, C.J. Aerosol-assisted delivery of precursors for chemical vapour deposition: Expanding the scope of CVD for materials fabrication. *Dalton Trans.* **2013**, *42*, 9406–9422. [[CrossRef](#)]
54. Powell, M.J.; Potter, D.B.; Wilson, R.L.; Darr, J.A.; Parkin, I.P.; Carmalt, C.J. Scaling aerosol assisted chemical vapour deposition: Exploring the relationship between growth rate and film properties. *Mater. Des.* **2017**, *129*, 116–124. [[CrossRef](#)]
55. Mazhar, M.; Hussain, S.M.; Rabbani, F.; Kociok-Kuhn, G.; Molloy, K.C. Synthesis, Thermal Decomposition Pattern and Single Crystal X-Ray Studies of Dimeric [Cu(dmae)(OCOCH₃)(H₂O)]₂: A Precursor for the Aerosol Assisted Chemical Vapour Deposition of Copper Metal Thin Films. *Bull. Korean Chem. Soc.* **2006**, *27*, 1572–1576. [[CrossRef](#)]